NUCL SCI TECH (2019) 30:32
https://doi.org/10.1007/s41365-019-0546-x

Simulation study of the dose and energy responses of FNTD personal neutron dosimetry

Yi-Hang Wang[1] · Qiang Li[2] · Li Chen[2] · Yong-Gang Yuan[1] · Tai-Ping Peng[1]

Received: 8 February 2018 / Revised: 25 May 2018 / Accepted: 30 June 2018 / Published online: 25 January 2019

Abstract The objective of this work was to use the Geant4 toolkit to perform simulation studies on the personal dose response of fluorescent nuclear track detectors (FNTDs). The entire structure of the FNTD response can be designed, and the detector's energy and dose responses can be optimized in a broad energy range (0.01 eV–20 MeV). In general, the detectors used ^{6}LiF and CH_2 converters that have high energy and high dose response at neutron energies lower than 10 eV and greater than 1 MeV, respectively. The method of least squares was used to optimize the dose response of $H^{*}(10)$ and the energy response corresponding to $\boldsymbol{R}_{\text{total}}$. The values of the optimized response of $H^{*}(10)$ lie between 0.8 and 1.4, corresponding to the energy ranges 0.01 eV–70 keV and 4–14 MeV, respectively. This occupies nearly eight out of the nine orders of the total energy range. Even though the optimized response of $\boldsymbol{R}_{\text{total}}$ is constrained between 0.89 and 1.1 in the energy range of 0.01 eV–20 MeV, it is suitable for obtaining the broad neutron spectrum of fluence with good accuracy.

Keywords FNTD · Geant4 · Al_2O_3/C, Mg · Personal neutron dose

This work was funded by the International Fusion Reactor Experiment Program (No. 2014GB112004).

✉ Yi-Hang Wang
lulifree@163.com

[1] Institute of Nuclear Physics and Chemistry, China Academy of Engineering Physics, Mianyang 621903, China

[2] China Institution for Radiation Protection, Taiyuan 030006, China

1 Introduction

Considering the broad energy spectra encountered in practical situations, accurately assessing the neutron dose absorbed by the human body is an extremely complex process, and there is almost no dosimetric method that covers such a wide range, i.e., between the energies of thermal neutrons and high-energy neutrons. The Landauer Corporation developed a fluorescence nuclear track detector (FNTD) that has demonstrated promising dosimetric performance for neutrons, protons, and other heavy charged particles [1–3]. This technology, which is based on the combination of the Al_2O_3/C, Mg single crystal, and confocal microscopy, can provide precise 3D information on ion tracks with resolution limited by optical diffraction [4, 5]. It has potential to replace the conventionally used CR-39 plastic nuclear track detector (PNTD) technology [5, 6] and is superior in many aspects compared to bubble detectors [7], thermoluminescence (TL) detectors, and optically stimulated luminescence (OSL) detectors [6, 8, 9].

The FNTD exhibits excellent efficiency for detection of heavy charged particles [10], allows multiple nondestructive readouts, does not require chemical post-processing treatment, and is capable of being erased and reused [11–14]. These make the FNTD superior for high-accuracy charged particle fluence measurements [11], clinical ion beam measurements [15], and an attractive candidate for a new-generation passive personal neutron dosimetry device. In the field of personal neutron dosimetry, many contributions have been made by the research group led by Akselrod [1–6, 16–18], which has studied this topic extensively. The main drawback of neutron radiation experiments is that they are time-consuming. At the same

time, it is rare to find a neutron field without a gamma contribution. As a solution, we applied the Monte Carlo simulation technique to study the neutron radiation energy and dose response of each personal FNTD.

Geant4 is a widely used Monte Carlo transport simulation toolkit. It can be applied in areas of high energy, nuclear, and accelerator physics, as well as in the medical and space sciences [19–21]. Along with the simulation of neutron transport in the detector material, the Geant4 toolkit can simulate the transport of protons or other charged particles. The energy and position of the particle are readily obtained, and this information can be used further to characterize the response of neutrons. Hence, in this work, we used the Geant4 procedure to design the neutron detector structure, test its energy and dose response corresponding to a wide energy range (0.01 eV–20 MeV), and propose an algorithm to characterize the energy spectrum of each personal neutron dosimetry.

2 Simulation design

2.1 Principle of detection

FNTDs are made of single crystals of aluminum (α-Al_2O_3) doped with carbon and magnesium ions. In contrast with Al_2O_3/C, which is used in thermally and optically stimulated luminescence dosimetry, this material has a high concentration of F_2^{2+} (2 Mg). These centers can convert to F_2^{+} (2 Mg) under radiochromic transformation. After radiation, the F_2^{+} (2 Mg) center is optically stimulated into one of its excited states by the laser scanning confocal microscope system. Ultimately, the electron returns to its ground state and fluoresces at 750 nm with a short lifetime of 75 $\pm$ 5 ns [3, 22, 23]. The intensity of the fluorescence depends on the local energy deposition of the ionizing radiation, which is used to characterize the radiation-induced signal.

Because neutrons are not directly ionizing in nature, to detect a neutron, it is necessary to mount a neutron converter on top of the Al_2O_3/C, Mg crystal. The personal neutron dosimeter can detect neutron energy in a broad range, i.e., 0.01 eV–20 MeV; however, different converter materials have to be used for detecting low- or high-energy neutrons. Polyethylene $(CH_2)_n$ contains a high concentration of hydrogen suitable for neutron detection [24] via elastic scattering. Consequently, the recoil proton escapes from the converter and penetrates inside the Al_2O_3/C, Mg crystal to produce ionized tracks. For the detection of thermal neutrons, the converter should be replaced with high thermal neutron capture cross-section materials, such as ^{6}LiF or ^{10}B. The corresponding nuclear reactions are as follows:

$$^6\mathrm{Li} + {}^1n(941\ \mathrm{barn}) \rightarrow {}^4\mathrm{He}(2.05\ \mathrm{MeV}) + {}^3\mathrm{H}(2.73\ \mathrm{MeV}), \quad (1)$$

$$^{10}\mathrm{B} + {}^1n(3837\ \mathrm{barn}) \rightarrow {}^4\mathrm{He}(1.47\ \mathrm{MeV}) + {}^7\mathrm{Li}(0.83\ \mathrm{MeV}) \quad (2)$$

The ranges of ^{4}He (2.05 MeV), ^{3}H (2.73 MeV), ^{4}He (1.47 MeV), and ^{7}Li (0.83 MeV) in Al_2O_3 are 4 μm, 24 μm, 3 μm, and 1.5 μm, respectively [5]. In our case, we selected ^{6}LiF as the thermal neutron converter material and maintained the ^{6}Li concentration at 92%, because the ^{4}He and ^{3}H generated by the nuclear reaction (Eq. 1) have higher energy and longer range in Al_2O_3/C, Mg than ^{4}He and ^{7}Li (Eq. 2). This choice is necessary for ensuring efficient detection by FNTD. As the contents of doped C and Mg are only 5000 ppm and 27 ppm, respectively, we supposed that Al_2O_3/C, Mg has the same particle stopping power as the Al_2O_3 material. In addition, polyethylene $(CH_2)_n$ was chosen as the fast neutron converter.

The radiation response ($\boldsymbol{M}$) is defined as the sum of tracks of the secondary particles ^{4}He, ^{3}H, and protons in the Al_2O_3/C, Mg material. During the simulation, these particles traverse the Al_2O_3/C, Mg material and the simulation software records properties of the particles such as energy, momentum, position, motor direction, time, and so on. However, some of these parameters do not need to be scored. Only the track length, direction, and position have to be taken into account to obtain the sum of tracks for all three secondary particles at any depth in the Al_2O_3/C, Mg material.

Additionally, we prepared an Al_2O_3/C, Mg crystal specimen covered with polytetrafluoroethylene (PTFE) to detect background signals, i.e., gamma signals of the mixed field environment. This approach is feasible because the PTFE does not contain hydrogen or ^{6}Li, which is not sensitive to neutron and can provide an electron equilibrium at the detector surface during gamma irradiation. The images obtained from the back of the PTFE only provide dose information for the photon, whereas those from the back of the ^{6}LiF or $(CH_2)_n$ provide dose information for both neutrons and photons. Hence, the combination of the three converter materials can be used for dosimetry in neutron and gamma mixed fields [25].

2.2 Construction of dosimetry setup

The overall structure of the FNTD must be as small as possible for applicability as a personal neutron dosimeter. We combined the design principles of a regular and an albedo detector structure and tested against different thicknesses of the converter to determine the detection efficiency of fast and thermal neutrons. An appropriate thickness of the converter must be chosen to ensure a

strong radiation-induced response at different energy levels between 0.01 eV and 20 MeV. Diagrams depicting the structure are shown in Fig. 1.

The overall size of the setup is 4.5 cm × 7 cm × 1 cm, and the entire structure is made of ^{10}B-containing polyethylene in order to absorb the thermal neutrons. There are ten pieces of FNTD with a size of 5 mm × 4 mm × 1 mm. These are marked with serial numbers 1–10 and magenta color. The detectors marked 1–6 are located at the front face of the dosimeter, and those marked 7–10 are located at the back. The FNTD surface is covered by a neutron converter material, ^{6}LiF, $(CH_2)_n$, CF_2, and these are marked with gray, lake blue, and brown color, respectively. The first and second detectors are covered by ^{6}LiF of different thicknesses, i.e., 100 μm, 1 mm, respectively; the third, fourth, and sixth are covered by polyethylene $(CH_2)_n$ of thicknesses of 10 μm, 1 mm, and 100 μm, respectively; the 5th detector is covered by 1 mm thick polytetrafluoroethylene (PTFE); the seventh, eighth, and tenth detectors, which are located in the albedo structure to detect the albedo neutron, are covered by ^{6}LiF of thicknesses of 100 μm, 10 μm, and 1 mm, respectively; and the ninth detector is covered with 100 μm thick polytetrafluoroethylene (PTFE).

For simulating the response of our FNTDs, the detector box is located at the center of the surface of a water tank, with a rectangular volume of 30 × 30 × 15 cm^3. The water tank plays the role of a human body. The radiation is applied using the General Particle Source (GPS) of the Geant4 procedure. We set a 2D square surface source with a parallel monoenergetic neutron beam emitted from a surface source and vertically incident on the tank's surface with a fluence of 0.933 × 10^7 cm^{-2}. The source particles have no bias and completely strike the detector. The initial position of each particle is given by the average of a distribution sampled in the area of the 2D surface source, shown as the green area in Fig. 2. The energy of monoenergetic neutrons is set to 30 monoenergetic points from 0.01 eV to 20 MeV. The number of particles that the GPS procedure can emit in a one-time simulation experiment is limited to 2^{31}, and the backscattering neutrons from the corner of the water tank have the possibility to enter the albedo part. Aiming to improve the beam fluence and reduce the simulation time, we initially irradiated the central area (15 × 15 cm^2) and subsequently the corners (7.5 × 7.5 cm^2). Because the nonirradiated area of the water tank during the initial irradiation is 12 times larger than the second irradiated area, the final data are the simulation result at the center summed with the simulation result at the corner multiplied by 12. A schematic diagram of the radiation process is shown in Fig. 2.

The radiation in the corners only affects the FNTD in the case of albedo, which is of less concern. According to the simulation data and the track number density, we found that neutron radiation at the corners causes a much lower response of the albedo detectors than that at the center. For instance, consider the value of the surface track number density of the albedo seventh detector. At an incident neutron radiation of 1 keV (the most sensitive energy point), despite a 12-fold enlargement, the corner takes up only 2.07% of the radiation response as compared to the center. Therefore, it is reasonable to assume that the other nonirradiated areas after the initial irradiation have approximately equal effectiveness to the albedo FNTD as the second irradiated area. To analyze the simulated data with sufficient accuracy, the final data are obtained by adding the 12-fold data from the corner irradiated to the data from the center irradiated.

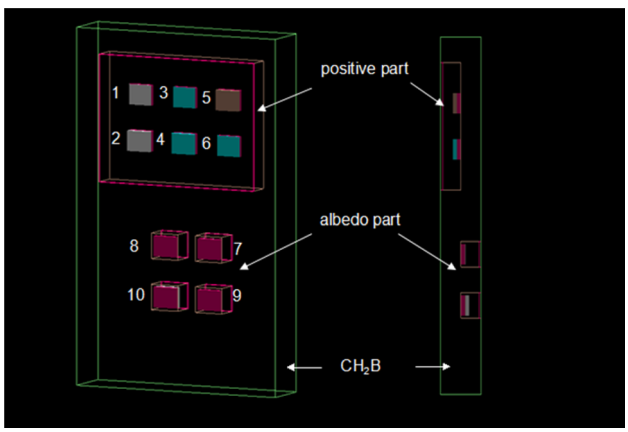

Fig. 1 (Color online) Structure of the personal neutron dosimetry setup

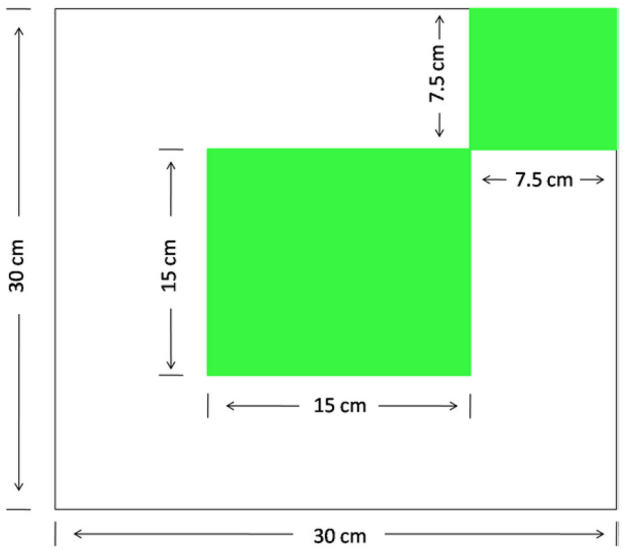

Fig. 2 Neutron radiation diagrams depicting the simulation

For the neutron response value ***M***, there are two important parameters that need to be considered. The first one is the track number of charged particles in the FNTD material at different depths, and the second is their corresponding total deposited energies. When a laser scanning confocal fluorescence imaging system is used to detect the irradiation, these two parameters correspond to the number of bright spots and their fluorescence strength integrals, respectively. In our work, we use the track numbers of proton, triton, and alpha particles to characterize the response of detectors covered by $(CH_2)_n$ and ^{6}LiF converters, respectively.

3 Results and discussion on simulation

3.1 Energy response of each detector

Because the alpha, triton, and proton particles make detectable tracks in the FNTD at a given neutron energy range, we can use the heavy charged particle number for the measurement of track numbers. We calculated the mean track number density of heavy charged particles at different depths inside the material for these detectors. These track number density responses corresponding to the surface were plotted against the values of neutron energy, as shown in Fig. 3.

Figure 3 depicts the track number density response at the surface for all FNTDs. For a clear comparison among the responses of all the detectors in one figure, we scaled up the data of all the $(CH_2)_n$ detectors by tenfold and those of all the albedo ^{6}LiF detectors by eightfold. We can see that the response obtained using the^{6}LiF converter has comparatively higher value for only the low neutron energy range, i.e., energies below 10 eV. The 100-μm ^{6}LiF detector has the highest response of all. The decisive factor is the thermal neutron (for an incident neutron energy lower than 1 eV) having a very high cross section with ^{6}Li atom, i.e., higher than 3000 b [26]. Another influence factor is the thickness of the ^{6}LiF; for lower thickness, there is less attenuation of neutrons, and more neutrons are available to react with ^{6}Li atoms to produce more alpha and triton particles that traverse the ^{6}LiF and penetrate the Al_2O_3/C, Mg material. There is a tendency of the most sensitive energy point of the detectors with the ^{6}LiF converter to increase with its thickness. The response of the detectors that used the $(CH_2)_n$ converter is sensitive only at the higher neutron energy range, i.e., more than 1 MeV. For thickness of $(CH_2)_n$ varying from 10 μm to 1 mm, there is a corresponding increase in the most sensitive energy peak position and signal strength. This occurs because the cross section of the neutrons reacting with the H atom is comparatively low (only a few barns), and the flux of neutrons transported through the $(CH_2)_n$ is kept almost constant. Hence, with increasing thickness of $(CH_2)_n$, more protons are produced from the collisions and penetrate into the Al_2O_3/C, Mg. The result of detectors using the albedo ^{6}LiF converter is higher response rates at the medium neutron energy range and lower rates at high- and low-energy ranges. The most sensitive energy peak positions are almost constant with increasing thickness of ^{6}LiF and are located near 1 keV. The responses of detectors with 10 μm and 100 μm thickness ^{6}LiF have almost the same value in the entire energy range, but they are significantly higher than the response of the detector with 1 mm thick ^{6}LiF. These results can be explained by the fact that almost all of the lower energy incident neutrons are absorbed by the CH_2B shell and are unable to reach the albedo ^{6}LiF. The high-energy incident neutrons have low cross section for the albedo detector ^{6}LiF, even though they backscatter from the water tank and the moderation of energy is not sufficient. Only the incident neutron energy

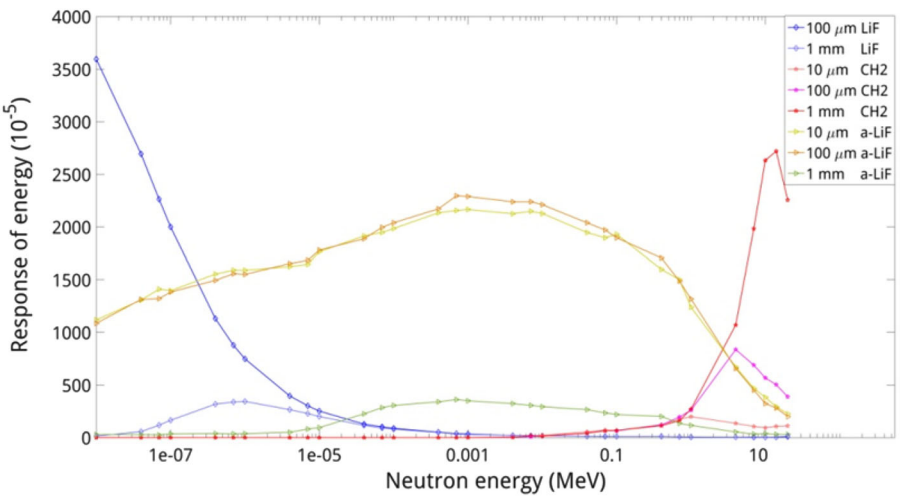

Fig. 3 (Color online) Response of neutron energy at the surface of the FNTDs

corresponding to the central energy range can have adequate moderation by backscattering from the water tank. At the same time, the thickness of albedo ^{6}LiF is very important for its detection efficiency. If it is too thick, it absorbs the moderated neutrons and the number of neutrons that can form efficient tracks decreases. On the other hand, if it is too thin, the number of lithium atoms is diminished. Because the values of the most sensitive energy of the detectors are distributed at different energy levels, it is suitable for characterizing neutrons belonging to a broad energy range.

We thoroughly investigated the track number density of the first (100 μm ^{6}LiF), fourth (1 mm CH_2), and seventh (100 μm α-^{6}LiF) detectors with normalized attenuation at increasing depths in Al_2O_3/C, Mg corresponding to the most sensitive energy peak positions, i.e., 0.01 eV, 14 MeV, and 1 keV, respectively. These results are shown in Fig. 4. We found that the normalized value of the track number density of the FNTD decreases with increasing depth in the Al_2O_3/C, Mg material, regardless of the FNTD being a normal structure or an albedo structure. The normalized values of the track number density for 100 μm ^{6}LiF are perfectly coincident with those corresponding to the 100 μm α-^{6}LiF, indicating that they have identical attenuation coefficients. This is because the reaction products of triton and alpha particles that penetrate the Al_2O_3/C, Mg material are almost the same with respect to their energy, angle, and momentum. The only difference is the number of triton and alpha particles, which is caused by the different number of neutrons. The normalized values of detector 4 [1 mm $(CH_2)_n$] decrease slowly with increasing depth. This occurs because the recoiled protons have comparatively lower mass, and the stopping power is lower than for triton or alpha particles. To measure the scanning depth after passage of radiation, confocal microscopy was used in the real experiment, and the parameter 1/e was incorporated to characterize the extent of change in the track number density. This parameter 1/e indicates the depth at which the track density decreases to ∼37% of its surface value, indicating that the sum of triton, alpha, and proton particles decreases with increasing depth in Al_2O_3/C, Mg materials and that the depth at which the sum particle density decreases to ∼37% compared to the surface is the 1/e depth. This concept was introduced by Sykora [18]. Both the 100 μm ^{6}LiF and the 100 μm α-^{6}LiF have identical 1/e depth of 7.85 μm, likely due to the reaction products having the same motion parameters. The 1/e depth of 1 mm $(CH_2)_n$ is 320 μm, as indicated in Fig. 4. A scan depth lower than this value will be more suitable when using the scanning confocal fluorescence imaging system in real experiments.

For a better understanding of the characterization of the track number density behind the converter, we studied the 1/e depth of detectors one, four, and seven under the dosimetric material surface corresponding to each sensitive energy range, as shown in Fig. 5. We found that the 1/e depth behind 100 μm ^{6}LiF exhibits little change with varying neutron energy compared with $(CH_2)_n$, irrespective of the structure being normal or albedo. Moreover, for some particular energy, both have the same value. This can be interpreted as indicating that although the number of reaction products of neutron reacting with ^{6}Li atom is influenced by the neutron energy via the change in reaction cross section, the energy of the nuclear reaction and the motion state of the reaction products remain the same. Therefore, the sum particles have approximately the same attenuation coefficients in Al_2O_3/C, Mg material and even have the same 1/e depth at some particular energy. The secondary particles of neutron reacting with ^{6}Li atoms are alpha and triton particles. Other reaction products can be ignored due to their low numbers. The 1/e depth behind the $(CH_2)_n$ increases with increasing energy of incident

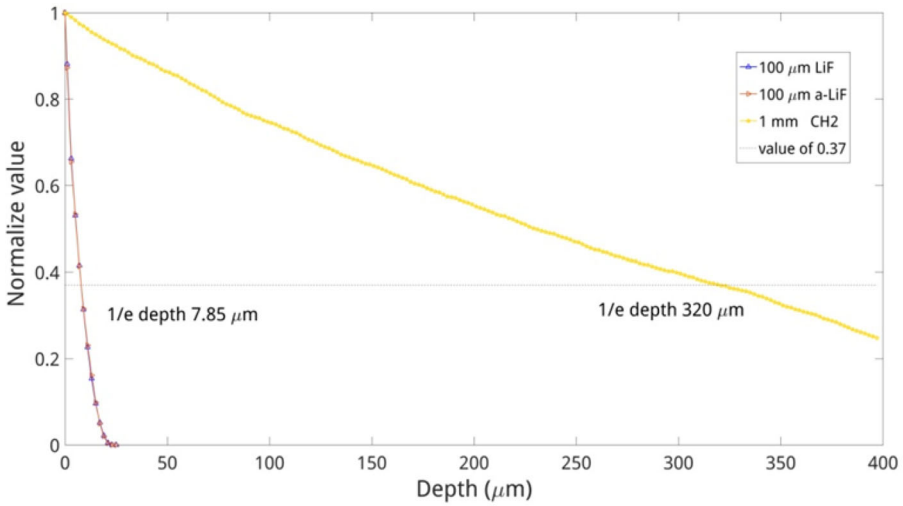

Fig. 4 (Color online) Graphical representation of the variation in track number density of detectors one, four, and seven with increasing depth in the Al_2O_3/C, Mg material. The neutron energies are 0.01 eV, 14 MeV, and 1 keV, respectively

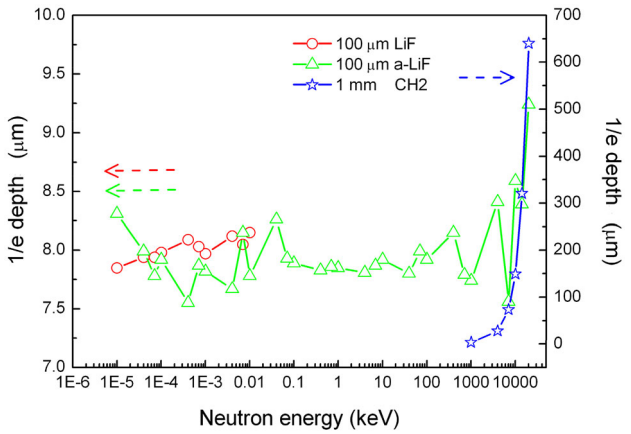

Fig. 5 (Color online) Plot of 1/e depth of the first, fourth, and seventh detector in each respective sensitive energy range

neutrons for values greater than 1 MeV. This result can be explained by the fact that more recoiled protons escape from a thick polyethylene converter with higher energies and larger ranges in collisions with higher energy neutrons. For incident neutron energies below 1 MeV, the energies of the recoiled protons are very low and the range is comparatively lower, while the 1/e depth is 3.3 μm for 1 MeV neutrons. As a result, most of them cannot escape the converter, and the 1/e depth is negligible. We recommend that the scanning depth in the real experiment be kept below the 1/e depth of the FNTD.

3.2 Algorithm used for characterization of $H^*(10)$

To assess the neutron personal dose using FNTD, we need to establish the connection of the response $\boldsymbol{M}$ of the FNTD with the neutron personal dose and model it with a simple algorithm. An assessment of the dose of neutron radiation received by the human body was performed using the ambient dose equivalent $H^*(10)$. The transition coefficient data points for $H^*(10)$ of 30 energy points between 0.01 eV and 20 MeV were calculated using the linear interpolation method and in accordance with the ICRP 74 report [27]. The relationship between $\boldsymbol{M}$ and $H^*(10)$ can be expressed as follows:

$$\boldsymbol{M} = \boldsymbol{R}\boldsymbol{\Phi} \tag{3}$$

$$H^*(10) = \boldsymbol{\mu}\boldsymbol{\Phi} \tag{4}$$

From formulae (3) and (4), we obtain

$$\frac{\boldsymbol{M}}{H^*(10)} = \frac{\boldsymbol{R}}{\boldsymbol{\mu}}. \tag{5}$$

The parameter μ is the conversion coefficient of neutron fluence to the neutron ambient dose equivalent $[H^*(10)]$, which is variable and changes with the neutron energy. Generally, the R/μ also changes with the neutron energy, making it difficult to assess $H^*(10)$ using a simple algorithm in the broad neutron energy radiation field. Optimizing the response R by the multiplicative coefficient makes the ratio R/μ approximately constant at every monoenergetic point. It is very convenient to assess $H^*(10)$ based solely on the total response $\boldsymbol{M}$, because it is not necessary to measure the neutron energy spectrum advance in this case. A single detector is sensitive to only a portion of the neutron energy in the range 0.01 eV–20 MeV. To obtain the neutron response for the entire range of energy, we have to combine the responses from different detectors. This is implemented by multiplying each of the responses by a coefficient and summing them. We assume that the fluence is the same for all components, which can be achieved in a real experiment if the detector is located at a sufficiently large distance from the source. The relation of the different parameters can then be represented as follows:

$$\begin{aligned}\boldsymbol{M}_{\text{total}} &= k_1\boldsymbol{M}_1 + k_2\boldsymbol{M}_2 + k_3\boldsymbol{M}_3 + k_4\boldsymbol{M}_4 + k_6\boldsymbol{M}_6 + k_7\boldsymbol{M}_7 \\ &\quad + k_8\boldsymbol{M}_8 + k_{10}\boldsymbol{M}_{10},\end{aligned} \tag{6}$$

$$\begin{aligned}\boldsymbol{R}_{\text{total}} &= \frac{M_{\text{total}}}{\Phi} \\ &= k_1\boldsymbol{R}_1 + k_2\boldsymbol{R}_2 + k_3\boldsymbol{R}_3 + k_4\boldsymbol{R}_4 + k_6\boldsymbol{R}_6 + k_7\boldsymbol{R}_7 \\ &\quad + k_8\boldsymbol{R}_8 + k_{10}\boldsymbol{R}_{10},\end{aligned} \tag{7}$$

$$\begin{aligned}&\frac{\boldsymbol{M}_{\text{total}}}{H^*(10)} \\ &= \frac{k_1\boldsymbol{R}_1 + k_2\boldsymbol{R}_2 + k_3\boldsymbol{R}_3 + k_4\boldsymbol{R}_4 + k_6\boldsymbol{R}_6 + k_7\boldsymbol{R}_7 + k_8\boldsymbol{R}_8 + k_{10}\boldsymbol{R}_{10}}{\mu}.\end{aligned} \tag{8}$$

The indexes of coefficient ($\boldsymbol{k}$), response ($\boldsymbol{M}$), and response density ($\boldsymbol{R}$) are in accordance with the indexes of FNTD detectors. In our case, the ratio $\boldsymbol{R}/\boldsymbol{\mu}$ is a matrix of dimension 30 × 8, and the unknown coefficient $\boldsymbol{k}$ is an 8 × 1 matrix. We build an overdetermined equation $\boldsymbol{A}\boldsymbol{k} = \boldsymbol{C}$, keeping $\boldsymbol{C}$ as a constant matrix of dimension 30 × 1 with fixed value of 1. Thus, the least squares solution of this overdetermined equation is the following:

$$\boldsymbol{k} = \left(\boldsymbol{A}^{\mathrm{T}} \cdot \boldsymbol{A}\right)^{-1}\boldsymbol{A}^{\mathrm{T}} \cdot \boldsymbol{C}. \tag{9}$$

The optimized coefficients k of these detectors are listed in Table 1.

Using the least squares method, we obtain the value of the optimized coefficients $\boldsymbol{k}$ for all components. The $\boldsymbol{k}$ value is low if the signal strength of one component is very high, and the $\boldsymbol{k}$ value is high if the signal strength of one component is very low. The purpose of the coefficients $\boldsymbol{k}$ is to make Eqs. (7) and (8) approximately equal to 1 at the 30 energy points between 0.01 eV and 20 MeV. However, the negative values of k only compensate the

Table 1 Values of response coefficients $k/10^5$

	k_1	k_2	k_3	k_4	k_6	k_7	k_8	k_{10}
Track number dose response	2.8×10^2	4.2×10^3	1.3×10^5	8.1×10^4	4.6×10^5	-6.3×10^3	5.3×10^3	2.1×10^4
Track number energy response	1.3×10^1	5.8×10^1	1.4×10^3	2.3×10^2	2.8×10^2	1.8×10^2	1.9×10^2	-1×10^2

contribution of other components used for optimizing the calculation.

3.3 $H^*(10)$ dose response of FNTD

We assessed the ability of the FNTD to characterize the personal neutron dose using the surface track number density of each detector divided by the $H^*(10)$'s transition coefficients $\boldsymbol{\mu}$. The $H^*(10)$ response of each detector can be obtained by using Eq. (5). The response of each detector plotted versus the neutron energy in Fig. 6. For a clear comparison of the dose response of all detectors in a single figure, we scaled up the data of all the $(CH_2)_n$ and albedo ^{6}LiF detectors 600-fold and eightfold, respectively. From Fig. 6, we can see that the dose responses of the ^{6}LiF converters are in accordance with their energy responses and are sensitive to incident neutron energies lower than about 10 eV. The dose response obtained using the $(CH_2)_n$ converter is mostly the same as the energy response shown in Fig. 3, and both are sensitive to neutron energies greater than about 1 MeV. However, there is a strong response near 10 keV, which may be caused by the change in the transition coefficient of $H^*(10)$. The highest discrepancy in the dose response corresponds to the albedo ^{6}LiF converter, and it has been amplified in the same way as the energy response. However, it has a significantly lower dose response in low- and high-energy ranges, particularly in the latter. This occurs because the transition coefficient of $H^*(10)$ has a higher value at the high-energy range, which is about 40-fold higher than that of the low-energy range. The responses of the 10- and 100-μm albedo ^{6}LiF converters are very similar, so we can improve the detector by using one thickness of albedo ^{6}LiF converter rather than both. The most sensitive energy range of these detectors is distributed at different energy levels, which is suitable for characterizing the broad energy range of personal neutron doses.

By multiplying the ratio $\boldsymbol{R/\mu}$ with the track number response coefficient (given in Table 1), we obtain the optimum normalized dose response of $H^*(10)$ with two valid digits, which is plotted against the neutron energy in Fig. 7. The entire curve has a relatively flat response at central and lower energy ranges and includes a part of the high-energy range; the maximum and minimum responses are 1.4 and 0.3, corresponding to the energies of 10 and 400 keV, respectively. The remaining values are bound between these two values in the whole energy range, i.e., 0.01 eV–20 MeV. For the portion of the response curve that is relatively flat, the neutron energy ranges included are 0.01 eV–70 keV and 4–14 MeV. These ranges are constrained between 0.8 and 1.4, occupying nearly eight out of nine energy levels. These properties are suitable for characterizing the personal neutron dose. The neutron with energy between 100 keV and 1 MeV has a comparatively low dose response of $H^*(10)$, making its detection difficult. However, only one out of nine energy levels (0.01 eV–

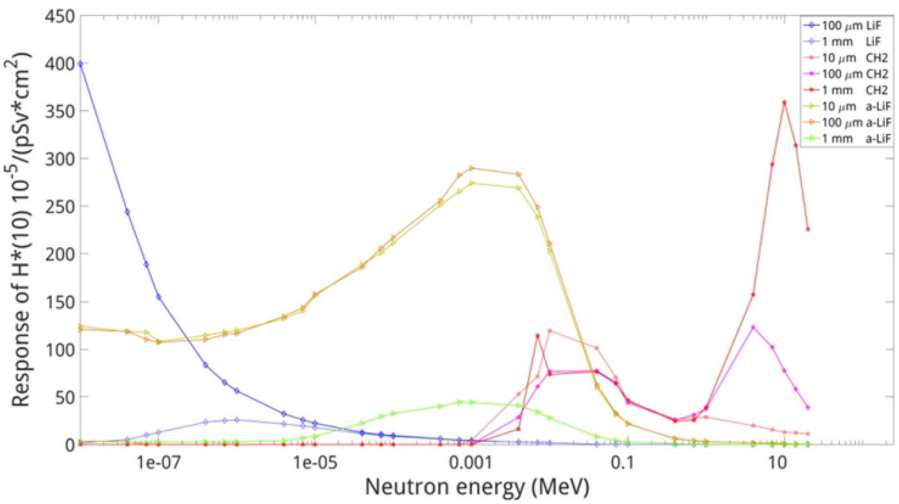

Fig. 6 (Color online) Graphical representation of the $H^*(10)$ response characterized by the surface track number density of each detector as a function of neutron energy

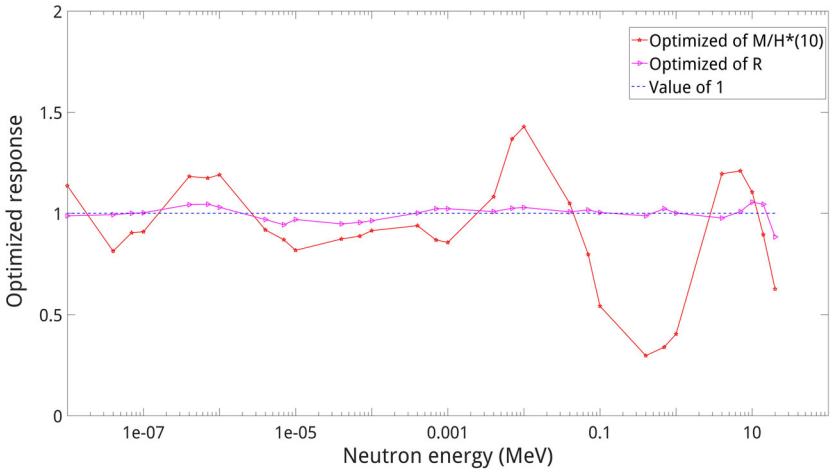

Fig. 7 Optimum normalized response of $H^*(10)$ and $\boldsymbol{R}_{\text{total}}$ characterized by the surface track number density of FNTDs

20 MeV) is required. Generally, by combining the track number density response of different detectors, we can obtain an exceedingly good $H^*(10)$ response for broad neutron energy spectra. The superior normalization of $\boldsymbol{R}_{\text{total}}$ is also kept with two valid digits and is shown in Fig. 7. This curve is comparatively flatter, and the values are constrained within 0.89–1.1 for the broad neutron energy spectra (0.01 eV–20 MeV). This indicates that we can obtain accurate neutron fluence in the broad energy neutron radiation range using our FNTD.

According to the simulation results of this paper, we attempted to simplify the structure of the FNTDs to satisfy the personal neutron dosimetry criterion in the best way possible. We chose the detectors covered by converters corresponding to 100 μm ^{6}LiF, 1 mm ^{6}LiF, 1 mm $(CH_2)_n$, and 100 μm α-^{6}LiF to redesign a new FNTD that has nearly the same flat response at different neutron energy ranges. Its overall size is reduced to 3.5 cm × 5.5 cm × 1 cm, and the structure is made of ^{10}B-containing polyethylene. There are six pieces of FNTD within it, each having a size of 5 mm × 4 mm × 1 mm. The detectors located at the front face are covered by ^{6}LiF with thicknesses of 100 μm and 1 mm, respectively, polyethylene $(CH_2)_n$ of 1 mm thickness, and PTFE of 1 mm thickness. The detectors located at the albedo part are covered by ^{6}LiF of 100 μm thickness and PTFE of 100 μm thickness. The entire size of the new simplified structure is smaller, and the structure is more convenient to use.

We used the track number density response of 100 μm ^{6}LiF, 1 mm ^{6}LiF, 1 mm $(CH_2)_n$, and 100 μm α-^{6}LiF and recalculated the optimized coefficients $\boldsymbol{k}$. By multiplying the $\boldsymbol{R}/\boldsymbol{\mu}$ of these detectors, we obtained the superior normalized $H^*(10)$ response and the $\boldsymbol{R}_{\text{total}}$, as shown in Fig. 8. The superior normalized value of $H^*(10)$ is constrained between 0.11 and 1.4. It is mostly flat in the energy ranges of 0.01 eV–70 keV and 4–14 MeV; however, in the range from 100 keV to 1 MeV, the response is more undulating. The superior normalized value of $\boldsymbol{R}_{\text{total}}$ is constrained between 0.71 and 1.1, close to 1 and in accordance with the normalized values shown in Fig. 7. These results indicate that the simplified FNTD retains the basic characteristics of all detectors.

4 Conclusion

The results of the simulation show that the FNTD technology has a very high potential for application in personal neutron dosimetry devices across the whole personal neutron dose monitoring energy range, i.e., from 0.01 eV to 20 MeV. We used the Geant4 toolkit to perform the simulations presented in this work. By adjusting the thicknesses of ^{6}LiF and $(CH_2)_n$ converter materials, we designed the entire structure of the FNTD to optimize the response energy range of the detected neutrons.

The energy response of the 100-μm ^{6}LiF detector was found to be superior for neutrons with energies lower than 10 eV, and the most sensitive energy point has a tendency to increase with increasing thickness of ^{6}LiF. However, the response magnitude shows an opposite tendency. The energy response of the $(CH_2)_n$ converter was found to be sensitive to high-energy neutrons, i.e., higher than 1 MeV, and the most sensitive energy point and response magnitude increase with increasing thickness of $(CH_2)_n$. The energy response of the albedo 100-μm ^{6}LiF converter results in a high and comparatively flat curve along the entire energy range. The most sensitive energy points are almost constant with increasing thickness of ^{6}LiF and are located at 1 keV. The responses of 10 μm α-^{6}LiF and 100 μm α-^{6}LiF have almost identical value along the entire energy range; however, both are significantly higher than those corresponding to 1 mm thick ^{6}LiF. The most sensitive energy points of these detectors are distributed across different energy levels, which is suitable for characterizing

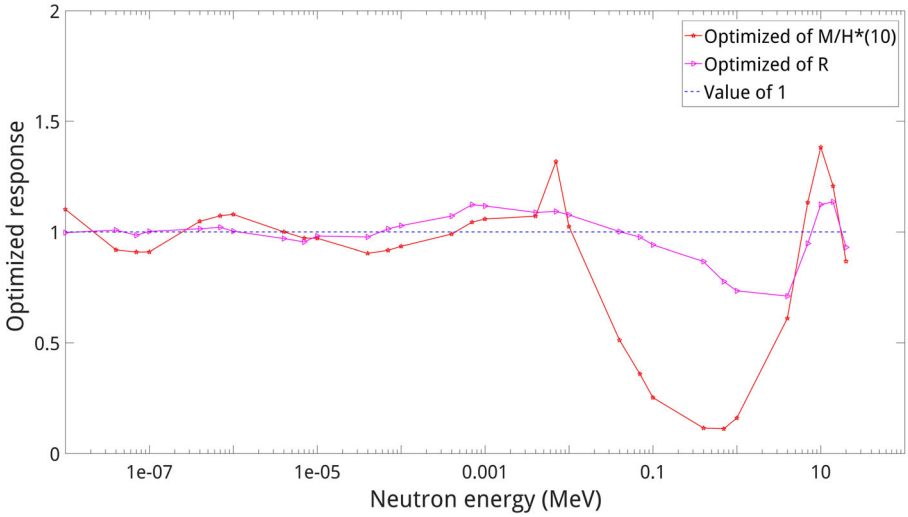

Fig. 8 (Color online) Optimum normalized response of $H^*(10)$ and $\boldsymbol{R}_{\text{total}}$ characterized by the surface track number density of the simplified FNTD

the broad spectrum neutron energy response. In the case of the personal neutron dose response of FNTD, the responses obtained using the ^{6}LiF and $(CH_2)_n$ converters are in accordance with the response curve shapes of the energy response. A significant discrepancy was found between the dose response curve shape for the albedo ^{6}LiF converter and its energy response. At the high-energy range, the value is significantly lower because the transition coefficient of $H^*(10)$ in the high-energy range is 40-fold higher than in the low-energy range.

After building an overdetermined equation $\boldsymbol{Ak} = \boldsymbol{C}$, the method of least squares was used to obtain the optimized coefficients $\boldsymbol{k}$ of $\boldsymbol{M}_{\text{total}}/H^*(10)$ and R_{total}. The optimum normalized response curve of $H^*(10)$ has a mostly flat region at the lower and central portions of the energy range and includes a portion of the high-energy range. The maximum and minimum responses are 1.4 and 0.3, corresponding to the 10 and 400 keV energy points, respectively. The other values are constrained between these two points in the entire energy range, i.e., 0.01 eV–20 MeV. For the mostly flat portion of the response curve, the neutron energy ranges include 0.01 eV–70 keV and 4–14 MeV, and the response values are constrained between 0.8 with 1.4, occupying nearly eight out of the nine energy levels in the range, making it appropriate for characterizing the personal neutron dose. If the neutron radiation field is deficient of neutrons in the energy range of 100 keV–1 MeV, calculating the $H^*(10)$ using the FNTDs will result in greater accuracy. The optimum normalized response R_{total} is almost equal to 1, and all values are constrained between 0.89 and 1.1. This is suitable for obtaining accurate neutron fluences between 0.01 eV and 20 MeV using our FNTD.

The estimation of dose in the 0.1–1 MeV region may be improved by measuring the neutron spectrum in this region using the recoil proton method [28]. The track length of the recoil proton corresponding to its energy combined with the recoil angle can be used to obtain the incident neutron energy. From the neutron spectrum, we can obtain $H^*(10)$ of this underestimation region by multiplying the fluence and dose conversion coefficients. This method will be investigated in a future study. In the last part of the study, we chose a detector with a typical response for various energy ranges, redesigned a new simplified FNTD structure with a smaller volume of $3.5 \times 5.5 \times 1$ cm^3, and investigated its energy and dose response. In future work, we aim to improve the methods used for dose response characterization further and also improve the miniaturization of the FNTDs.

References

1. M.G. Akselrod, M.S. Akselrod, E.R. Benton et al., A novel Al_2O_3 fluorescent nuclear track detector for heavy charged particles and neutrons. Nucl. Instrum. Method B **247**, 295–306 (2006). https://doi.org/10.1016/j.nimb.2006.01.056
2. M.S. Akselrod, R.C. Yoder, M.G. Akselrod, Confocal fluorescent imaging of tracks from heavy charged particles utilizing new Al_2O_3:C, Mg crystals, Mg crystals. Radiat. Prot. Dosim. **119**, 357–362 (2006). https://doi.org/10.1093/rpd/nci664
3. M.S. Akselrod, A.E. Akselrod, New Al_2O_3:C, Mg crystals for radio photo luminescent dosimetry and optical imaging. Radiat. Prot. Dosim. **119**, 218–221 (2006). https://doi.org/10.1093/rpd/nci663
4. O.S. Gabriel, A.F. Felisberto, H.M. Conor et al., Nanoscale measurements of proton tracks using fluorescent nuclear track detectors. Med. Phys. **43**, 2485–2490 (2016). https://doi.org/10.1118/1.4947128
5. G.J. Sykora, M. Salasky, M.S. Akselrod, Properties of novel fluorescent nuclear track detectors for use in passive neutron dosimetry. Radiat. Meas. **43**, 1017–1023 (2008). https://doi.org/10.1016/j.radmeas.2007.12.038

6. M.S. Akselrod, V.V. Fomenko, J.A. Bartz et al., Automatic neutron dosimetry system based on fluorescent nuclear track detector technology. Radiat. Prot. Dosim. **161**, 86–91 (2014). https://doi.org/10.1093/rpd/nct293
7. F. d'Ericco, Radiation dosimetry and spectroscopy with superheated emulsions. Nucl. Instrum. Methods B. **184**, 229–254 (2001). https://doi.org/10.1016/s0168-583x(01)00730-3
8. E.G. Yukihara, R. Gaza, S.W.S. McKeever et al., Optically stimulated luminescence and thermoluminescence efficiencies for high-energy heavy charged particle irradiation in Al_2O_3:C. Radiat. Meas. **38**, 59–70 (2004). https://doi.org/10.1016/s1350-4487(03)00251-8
9. J.C.R. Mittani, A.A.R. Silva, F. Vanhavere et al., Investigation of neutron converters for production of optically stimulated luminescence (OSL) neutron dosimeters using Al_2O_3:C. Nucl. Instrum. Methods B. **260**, 663–671 (2007). https://doi.org/10.1016/j.nimb.2007.03.083
10. G.J. Sykora, M.S. Akselrod, E.R. Benton et al., Spectroscopic properties of novel fluorescent nuclear track detectors for high and low LET charged particles. Radiat. Meas. **43**, 422–426 (2008). https://doi.org/10.1016/j.radmeas.2007.11.009
11. J.M. Osinga, M.S. Akselrod, R. Herrmann et al., High-accuracy fluence determination in ion beams using fluorescent nuclear track detectors. Radiat. Meas. **56**, 294–298 (2013). https://doi.org/10.1016/j.radmeas.2013.01.035
12. J.M. Osinga, I. Ambrozova, K.P. Brabcova et al., Single track coincidence measurements of fluorescent and plastic nuclear track detectors in therapeutic carbon beams. J. Instrum. **9**, 4–13 (2014). https://doi.org/10.1088/1748-0221/9/04/p04013
13. M.S. Akselrod, G.J. Sykora, Fluorescent nuclear track detector technology—a new way to do passive solid state dosimetry. Radiat. Meas. **46**, 1671–1679 (2011). https://doi.org/10.1016/j.radmeas.2011.06.018
14. M.S. Akselrod, V.V. Fomenko, J.A. Bartz et al., FNTD radiation dosimetry system enhanced with dual-color wide-field imaging. Radiat. Meas. **71**, 166–173 (2014). https://doi.org/10.1016/j.radmeas.2014.05.026
15. S. Greilich, J.M. Osinga, M. Niklas et al., Fluorescent nuclear track detectors as a tool for ion-beam therapy research. Radiat. Meas. **56**, 267–272 (2013). https://doi.org/10.1016/j.radmeas.2013.01.033
16. M.S. Akselrod, Fundamentals of materials, techniques, and instrumentation for OSL and FNTD dosimetry. AIP. Conf. Proc. **1345**, 274–302 (2011). https://doi.org/10.1063/1.3576173
17. G.J. Sykora, M.S. Akselrod, M. Salasky et al., Novel Al_2O_3:C, Mg fluorescent nuclear track detectors for passive neutron dosimetry. Radiat. Prot. Dosim. **126**, 278–283 (2007). https://doi.org/10.1093/rpd/ncm058
18. G.J. Sykora, M.S. Akselrod, F. Vanhavere, Performance of fluorescence nuclear track detectors in mono-energetic and broad spectrum neutron fields. Radiat. Meas. **44**, 988–991 (2009). https://doi.org/10.1016/j.radmeas.2009.10.027
19. S. Agostinelli, J. Allison, K. Amako et al., Geant4—a simulation toolkit. Nucl. Instrum. Methods Phys. Res. **506**, 250–303 (2003). https://doi.org/10.1016/s0168-9002(03)01368-8
20. J. Allison, K. Amako, J. Apostolakis et al., Geant4 developments and applications. IEEE. Trans. Nucl. Sci. **53**, 270–278 (2006). https://doi.org/10.1109/TNS.2006.869826
21. J. Allison, K. Amako, J. Apostolakis et al., Recent developments in Geants. Nucl. Instrum. Methods Phys. Res. **835**, 186–225 (2016). https://doi.org/10.1016/j.nima.2016.06.125
22. M.S. Akselrod, A.E. Akselrod, S.S. Orlov et al., Fluorescent aluminum oxide crystals for volumetric optical data storage and imaging application. J. Fluoresc. **13**, 503–511 (2003). https://doi.org/10.1023/b:jofl.0000008061.71099.55
23. M.S. Akselrod, S.S. Orlov, G.M. Akselrod, Bit-wise volumetric optical memory utilizing two-photon absorption in aluminum oxide medium. Jpn. J. Appl. Phys. **43**, 4908–4911 (2004). https://doi.org/10.1143/JJAP.43.4908
24. F.H. Attix, *Introduction to Radiological Physics and Radiation Dosimetry*, vol. 27 (Wiley, New York, 1986), pp. 111–123. https://doi.org/10.1002/9783527617135
25. G.J. Sykora, M.S. Akselrod, Novel fluorescent nuclear track detector technology for mixed neutron–gamma fields. Radiat. Meas. **45**, 594–598 (2010). https://doi.org/10.1016/j.radmeas.2010.01.037
26. D.F. Tian, W.L. Sun, *Excitation Functions in Neutron-Induced Reactions* (National Defense Industry Press, Beijing, 2006). **(in Chinese)**
27. ICRP, *ICRP Publication 74[M]* (Pergamon Press, Oxford, 1996)
28. J. Wang, X.L. Lu, Y. Yan et al., Study of an unfolding algorithm for D–T neutron energy spectra measurement using a recoil proton method. Chin. Phys. C. **39**, 59–63 (2015). https://doi.org/10.1088/1674-1137/39/7/076201